Optics Letters

Shape-adapting panoramic photoacoustic endomicroscopy

KEDI XIONG,[1,2] WEI WANG,[2] TING GUO,[2] ZHEN YUAN,[3] AND SIHUA YANG[1,2,*]

[1]MOE Key Laboratory of Laser Life Science and Institute of Laser Life Science, South China Normal University, Guangzhou 510631, China
[2]College of Biophotonics, South China Normal University, Guangzhou 510631, China
[3]Bioimaging Core, Faculty of Health Sciences, University of Macau, Taipa, Macau SAR 999078, China
*Corresponding author: yangsh@scnu.edu.cn

Received 28 March 2019; revised 26 April 2019; accepted 26 April 2019; posted 29 April 2019 (Doc. ID 363592); published 22 May 2019

Photoacoustic (PA) endoscopy (PAE) has exhibited potential for providing the complementary contrast to available optical endoscopy methods, particularly for deep vessel imaging. In this Letter, a prototype PA endoscope with shape imaging was developed for the first time, to the best of our knowledge, which utilized the water-balloon-based adapting boundary recognition technique to extract panoramic vascular networks layer by layer. Interestingly, the PA endoscopic probe consists of a low-colored, high-transparency balloon and a 20 MHz ultrasound transducer, which can identify the boundary and construct holonomic vascular networks layer by layer based on the boundary of the balloon with enhanced axial resolution. Phantoms and *in vivo* rabbit colorectal tests were performed to characterize and inspect the PAE performance. The imaging results demonstrated that the shape-adapting panoramic PAE opens a new avenue for improving the endoscopic imaging capability, holding potential into the colorectal disease detection and guiding treatment in clinical applications.

https://doi.org/10.1364/OL.44.002681

Cancer of the colorectum is one of the most common malignant tumors, ranked third among all cancers globally after lung and breast cancer [1]. The high mortality rate is related to the pathophysiology mechanism of this disease, which can progress silently for a long time period before the appearance of clearly detectable symptoms. To date, the survival rate of colorectum cancer is low, since it most likely has progressed to advanced stages and spread to other parts of the body. In particular, the growth of the tumor consumes large amounts of nutrients supplied by the blood vessels. As such, tumor margins and surrounded vascular structures are clinically relevant, which might provide diagnosis information for assessing the disease stage or progression, and guiding treatment. However, previous studies showed that the white light endoscopy cannot capture the early epithelial dysplastic changes, as well as vascular morphology changes in distinct layers due to the lack of depth-resolved information and limited vascular lesion sensitivity [2]. As a result, it is essential to improve the imaging sensitivity to detect vascular network changes using a novel endoscopy technique. Importantly, endoscopic ultrasonography showed that it can detect colorectum tumors, although it cannot identify the superficial layer structure due to its poor tissue contrast in the case that dysplasia or early-stage tumors are present. In addition, optical endoscopic imaging modalities such as endoscopic optical coherent tomography [3], narrow band imaging endoscopy [4], and confocal laser endomicroscopy [5] have been developed, which can detect tissue with high resolution and high sensitivity. However, these high-resolution techniques are unable to image tissue beyond a 1 mm depth due to the strong optical scattering.

In contrast, photoacoustic endoscopy (PAE) that embodies PA imaging in a miniaturized probe can provide high resolution imaging of internal organs with optical absorption contrast based on the endogenous optical chromophore of abundant biomolecules, including DNA, melanin, and hemoglobin [6–8]. PAE enabled label-free imaging of complex morphology and physiological information such as microvascular structures and blood oxygen saturation [9–11], which have shown the potential to reveal complementary contrast to optical endoscopy methods, particularly for deep vessel imaging within tissue. Thus, PA endoscopy is a potentially powerful tool for colorectal (CR) and gastrointestinal (GI) tract imaging to visualize the vessels from superficial capillary to profound aorta [12–15], especially in accurate detection of tumor [16] angiogenesis related to morphological change of microvascular network at a high resolution [17,18]. Although a number of groups have developed small PA endoscopic probes [19,20] and partly achieved vessel imaging [21,22], a large variation in CR and GI wall distance results in that the holonomic vascular network distributed at distinct layers cannot be extracted and displayed separately in an equidistant maximum amplitude project mode, which restricts the accurate assessment of the vascular network in endoscopy.

In this Letter, seeking to construct holonomic vascular networks layer by layer in endoscopic imaging mode, for the first time, to the best of our knowledge, we designed a prototype PA endoscope using a balloon for shape-adapting imaging. The uniquely designed PAE used a water-balloon to stick to the

CR wall, providing pure and airless water coupling between the transducer and CR wall. Meanwhile, the use of a red-transparent balloon provided a precise and continuous boundary of CR wall, by which the vascular networks were precisely located and extracted layer by layer based on the PA signal of the balloon. Therefore, the shape-adapting PAE will provide more accurate information of vessels in clinical assessment and help guide the detection and treatment of CR diseases.

Figure 1(a) shows a schematic of the PA endoscopic system. Light from a 532 nm laser (DTL314, Laser-export, Russia) with a pulse repetition rate of 8 kHz was reshaped by an iris (GCM-5702M, Daheng Optics) and filtered by an optical spatial filter system. The filtered laser beam was coupled into a single-mode fiber (SMF) via a coupler (PAF-X-7-A, Thorlabs). The output laser was collimated and focused by two lenses. The pulse energy was 1.2 μJ, and the pulse width was 7 ns. The ultrasound transducer was connected to an electric rotary joint; the PA signals were amplified by a low noise amplifier (LNA-650, Rfbay Inc.) and digitized at 100 MS/s and 14 bit resolution (M3i 4110, spectrum, Inc). Recorded signals were digitally bandpass filtered based on the transducer bandwidth. 4000 A-lines were acquired with an angular resolution of 0.09° to reconstruct a B-scan image based on GPUs, and a median filtering was used to improve signal-to-noise ratio (SNR). The detailed structure of the probe is presented in Fig. 1(b). An incorporate ultrasonic probe shell was fabricated to mount the components. A customized 45° rod mirror is fixed in the hole of the probe shell to reflect the focused laser beam to the target. A customized focused ultrasonic transducer with a center frequency of 20 MHz and a bandwidth of 90% was used to detect PA signals. The transducer's element is a ring with an outer diameter of 3 mm and an inner diameter of 1.2 mm, which was installed in the side hole of the probe shell. A rod lens (1.2 mm diameter, 1.5 mm length) was put into the hole of a transducer cover 1 mm; the epoxy resin glue was daubed in the side wall and then the rod lens was completely pushed into the hole, and was coaxially fixed in transducer backing as the optical window to keep the laser illuminating and against the coupling leaking. Two bearings formed a rotary junction near the fiber capillary inside the probe shell to provide a free rotation only to the probe shell, separating it from the SMF. The incorporate transducer shell enables the ultrasonic transducer to remain relatively stationary with the reflective surface. Via the incorporate shell, the endoscope can achieve a rotating scanning with an angular field-of-view (FOV) of 360° and an efficient overlap of the light illumination and acoustic reception. To encapsulate all endoscope components, we fabricated the probe housing from a plastic material tube, remaining stationary, the end of which is the water injection hole and air exhaust hole. Two channels penetrated the wall of the tube to connect the injection hole and exhaust hole. A groove is designed at the top of the tube to bind the water-balloon. The red-transparent balloon is made of natural latex, with a thickness of ~50 μm, which can be adapted to the shape of the cavity. Figure 1(c) shows the photograph of the probe.

Figure 2 shows the characterization results of a surgical blade phantom as the distribution of the surgical blade is illustrated in Fig. 2(a). Figure 2(b) exhibits optical beam intensity distribution at the focal distance, detected by a laser beam analyzer, and the full width at half-maximum (FWHM) of the measured laser beam is about 23 μm. Figure 2(c) shows the radial maximum amplitude projection (RMAP) image of the surgical blade, which is covered by 480 B-scans with a step size of 15 μm. The sharp edge of the surgical blade was imaged to obtain the edge spread function (ESF), which was further used to derive the line spread function (LSF). Figure 2(d) presents the cross-sectional profiles of the imaged blade edge along

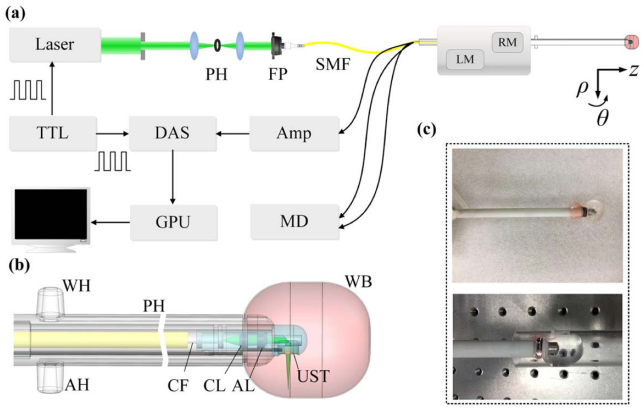

Fig. 1. Schematic of the system. (a) Schematic illustration of the imaging setup. PH, pinhole; FP, fiber port; DAS, data acquisition system; AMP, amplifier; GPU, graphics processing unit; MD, motor driver; RM, rotate motor; LM, linear motor; z represents the scanning direction; ρ means the radial distance; θ presents the scanning angle. (b) Structure of the probe. WH, water hole; AH, air hole; PH, plastic housing; WB, water-balloon; CF, ceramic ferrule; CL, collimating lens; AL, aspheric lens; UST, ultrasonic transducer. (c) Photograph of the probe.

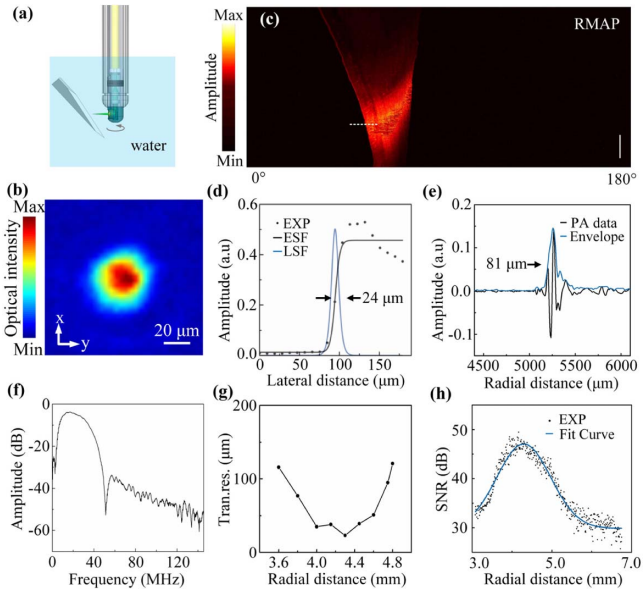

Fig. 2. Evaluation of the system performance. (a) Schematic diagram of the experiment. (b) Measured optical intensity distribution of laser beam at the focus. (c) RMAP PA image of blade formed by 480 B-scans. (d) FWHM of the Gaussian-fitted lateral profiles of the blade edge. (e) Typical PA signal and Hilbert-transformed signal. (f) Bandwidth of the transducer. (g) Transverse resolution change along the depth. (h) Sensitivity distribution versus the radial distance. FWHM, full width at half-maximum; EXP, experimental data; ESF, edge spread function; LSF, line spread function. Scale bar: 1 mm.

the dashed line in Fig. 2(c). Based on the LSF, the experimental lateral resolution of the system appeared to be ~24 μm, which is consistent with the measured FWHM of the optical beam intensity shown in Fig. 2(b). In the radial direction, the resolution depends on the bandwidth and center frequency of the ultrasonic transducer. Figure 2(e) shows a Hilbert-transformed signal of a typical depth-resolved PA signal as the radial LSPs of the target located at the focal point. The FWHM of the radial profile is ~81 μm, which is lower than the theoretical radial resolution (73 μm) [23]. Figures 2(f) and 2(g) present the bandwidth of the ultrasonic transducer and resolution change along the depth. The laser beam and ultrasound beam diverge with distance from the probe. SNR values (the ratio between the highest intensity values and the standard deviation of background) along the radial distance as the sensitivity distribution is depicted in Fig. 2(h). It can be seen that the optimal sensitivity distance is 4.1 mm, which is close to the optical focal distance of 4.3 mm. The output energy of probe is 1.2 μJ (0.95 uJ after the balloon), which yields a surface fluence of ~18 mJ/cm^2, below the ANSI safety limit (20 mJ/cm^2) [24].

To further extract the boundary of the water-balloon, the system noise amplitude and PA signal amplitude of the water-balloon were measured to determine the threshold value. 4000 maxima of A-lines were depicted in Fig. 3(a), and we set the threshold value to 0.06 to eliminate false peak of noise, so that the extracted signal peak comes from the water-balloon rather than the noise. Meanwhile, Fig. 3(b) presents the PA signal amplitudes of the water-balloon along the depth direction, which are above the threshold value. Thus, the distances of the boundary were accurately calculated by the first signal peak above the threshold value on the condition that the amplitudes of the background signals are less than those of the water-balloon. In signal processing, a smoothing algorithm is used to filter the strong peak interference from individual pulse noise.

A phantom experiment of a leaf was conducted to evaluate the performance of the system. Two layers of leaf covered together and around a transparent tube. The probe was inserted in the tube. Figure 4(a) shows the RMAP image of the covered leaf in an *en face* plane. Figure 4(b) shows a PA B-scan image of a leaf in 180° angular FOV transformed to a Cartesian coordinate system. It can be seen that the radial distance of the boundary covered more than 2 mm. Therefore, the MAP image extracted by equal depth shown in Fig. 4(c) presents a narrow FOV, which is not applicable to extract the holonomic vascular networks in an endoscopic imaging mode. Figures 4(d) and 4(e) present the images of a leaf in the first layer and second layer, respectively, which show an accurate representation of the

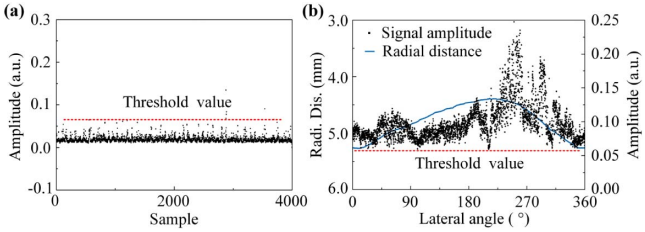

Fig. 3. Boundary extraction of the system. (a) 4000 system noise samples. (b) PA signal amplitude of the water-balloon versus the distance from the transducer and the boundary distance of the water-balloon.

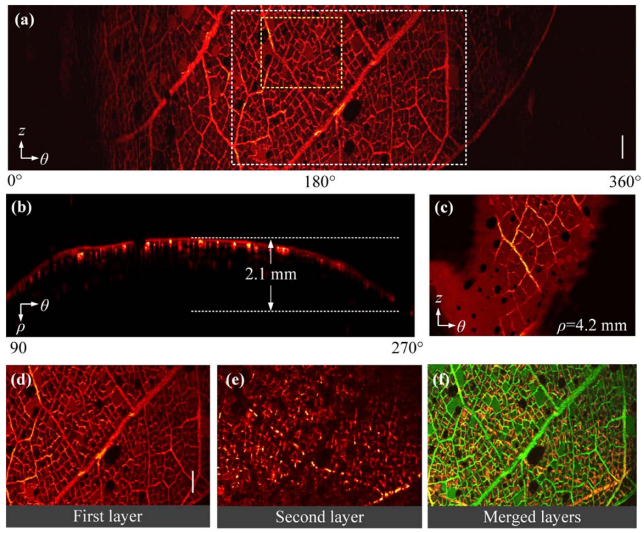

Fig. 4. Imaging evaluation of the leaf phantom. (a) RMAP of leaf phantom. (b) PA B-scan image of 180° angular FOV transformed to a Cartesian coordinate system. (c) RMAP image of a yellow dashed box at radial distance = 4.2 mm. (d) RMAP image of the first layer of the leaf phantom. (e) RMAP image of the second layer of the leaf phantom. (f) RMAP image of merged layers. Scale bar: 1 mm.

leaf structure. Notice that the leaf structure appeared to have massive discontinuity in Fig. 4(e) due to the opacity of leaf in the first layer. Figure 4(f) shows a MAP image of the leaf structure. It illustrates the depth-dependent nature of the data; the shallow layer appears in green, and the deep layer appears in orange.

To further demonstrate the feasibility of the system on *in vivo* biological tissues, we imaged the colorectum of a rabbit with the setup shown in Fig. 1(a). Before the experiments, we anesthetized the animal by administrating a sodium pentobarbital (30 mg/kg) to keep it motionless and placed it on a heating pad to maintain the body temperature at 37°C. Once the animal was properly positioned, we inserted the endoscope through the anus, advanced it ~5 cm, and performed 3D imaging with a pullback speed of ~30 μm/s. During imaging, anesthesia was maintained with 2–3% isoflurane supplied through a nose cone. Figure 5(a) shows a histology image of the colorectum, which exhibits that the detailed structure of the colorectum included three layers and vessels. Figure 5(b) presents a cross-sectional PA image in a FOV of 90°. Vessels with different sizes can obviously be observed at three depths. Figures 5(c)–5(e) present the 3D images of vascular structures in the muscularis propria and serosa, mucosa, and submucosa, respectively. Figure 5(f) shows the RMAP image of the CR wall, which is capable of resolving the dense vascular network. Figures 5(g)–5(i) show the enlarged view of the dashed boxes in Figs. 5(c)–5(e), respectively. As shown in Figs. 5(g)–5(i), different morphological distributions of vascular networks at three depths can be obviously observed, respectively, separated by the thicknesses of 225, 165, and 300 μm. Figure 5(g) presents a vascular network in the muscularis propria and serosa, the artery, and vein from the mesentery pass through the serosa to the muscular propria, which produces branches of arteries and veins of a large size perpendicular to the scanning direction. The diameter of the vessel along the white arrow 1 is around

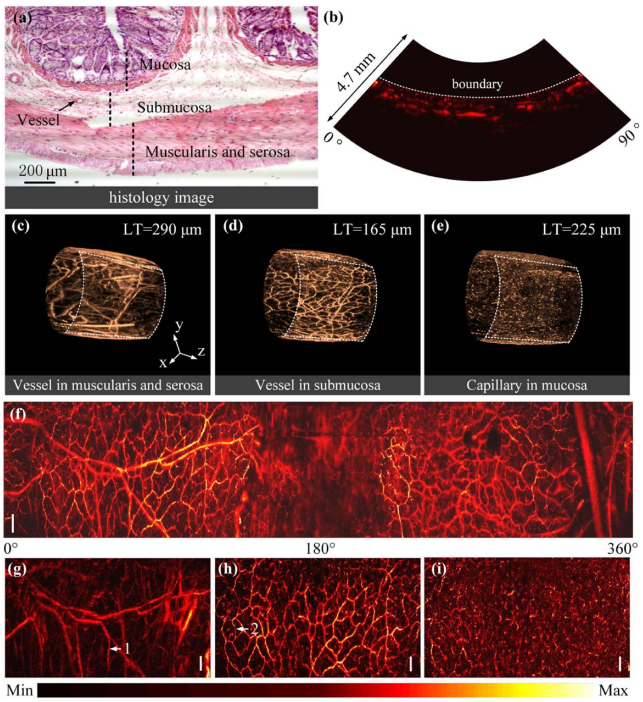

Fig. 5. PA imaging of an *in vivo* colorectum. (a) Histology image of a colorectum. (b) Cross-sectional PA image corresponding to the histology image. (c)–(e) 3D images of a vascular network in serosa and muscularis, submucosa, and mucosa, respectively. (f) RMAP image of a colorectum. (g)–(i) RMAP images of the dashed boxes in (c)–(e), respectively. LT, layer thickness. Scale bar: 1 mm.

127 μm. Figure 5(h) shows the submucosa layer, which is a deeper connective tissue layer to support the mucosa. The arteries and veins pass through muscularis propria to the submucosa, and produce a vascular network, forming a mesh structure. The diameter of the venule along the white arrow 2 is around 41 μm. As shown in Fig. 5(i), a massive compact punctate structure can be observed, representing the capillaries in a mucosa layer. Due to the deficiency of the lateral resolution and the defocused scanning, the capillary cannot be clearly identified. It is noted that some vascular distortion was caused by breathing and the imaging speed of 2 Hz.

In summary, we designed a prototype PA endoscope for shape-adapting panoramic PA endoscopic imaging, and proposed a water-balloon-based boundary recognition to extract the holonomic vascular networks layer by layer in an endoscopic imaging mode. By using a red-transparent water-balloon, the system will obtain a pure and airless coupling medium between the transducer and CR wall. However, some deficiencies should be resolved before it can be translated to clinical applications. First, the limited length of the depth-of-focus (DOF) results in the heterogeneity of the lateral resolution at the contact boundary. For this, some methods of enhancing DOF will be used to improve the resolution deterioration, as the radial depth increases. Although we have achieved high-resolution in lateral direction, the radial resolution is still limited by the acoustic parameters of the transducer. Therefore, a high center frequency transducer with an ultra-wide bandwidth will be used to improve the radial resolution to clearly differentiate blood vessels in different finer layers of the colorectum. Moreover, the high-resolution endoscopic imaging reduces the imaging speed, as that the repetition rate of the laser is only 8 kHz. In the future, a laser source with a higher repetition rate will be utilized to increase the imaging speed and mitigate motion artifacts caused by breathing. Although the water pressure may result in a tiny change of the vascular morphological structure, in fact, the vascular morphology of tumors is dense and disordered, which is quite different from the morphology of normal vascular networks. Therefore, a tiny change of normal vascular morphological structure has no impact on diagnosing a tumor. Generally, the present work will help guide the detection and treatment of CR diseases and provide more clinically useful information.

Funding. National Natural Science Foundation of China (NSFC) (11604105, 11774101, 61627827, 61822505, 81630046); The Science and Technology Planning Project of Guangdong Province, China (2015B020233016); The Science and Technology Youth Talent for Special Program of Guangdong, China (2015TQ01X882).

REFERENCES

1. S. McGuire, Adv. Nutr. **7**, 418 (2016).
2. R. Lambert and J. F. Rey, Endoscopy **33**, 348 (2001).
3. D. C. Adler, Y. Chen, R. Huber, J. Schmitt, J. Connolly, and J. G. Fujimoto, Nat. Photonics **1**, 709 (2007).
4. S. Han, A. Hsu, and W. Y. Wassef, Curr. Opin. Gastroenterol **32**, 492 (2016).
5. K. Karia and M. A. Kahaleh, Clin. Endosc. **49**, 462 (2016).
6. V. Ntziachristos, Nat. Methods **7**, 603 (2010).
7. L. V. Wang and S. Hu, Science **335**, 1458 (2012).
8. A. Taruttis and V. Ntziachristos, Nat. Photonics **9**, 219 (2015).
9. J. Yang, C. Favazza, R. Chen, J. Yao, X. Cai, K. Maslov, Q. Zhou, K. Shung, and L. Wang, Nat. Med. **18**, 1297 (2012).
10. A. Hussain, W. Petersen, J. Staley, E. Hondebrink, and W. Steenbergen, Opt. Lett. **41**, 1720 (2016).
11. W. T. Zhou, Z. J. Chen, S. H. Yang, and D. Xing, Opt. Lett. **42**, 2145 (2017).
12. C. Li, J. Yang, R. Chen, C. Yeh, L. Zhu, K. Maslov, Q. Zhou, K. Shung, and L. Wang, Opt. Lett. **39**, 1473 (2014).
13. J. Yang, C. Favazza, J. Yao, R. Chen, Q. Zhou, K. Shung, and L. Wang, Plos One **10**, e0120269 (2015).
14. J. Yang, C. Li, R. Chen, B. Rao, J. Yao, C. Yeh, A. Danielli, K. Maslov, Q. Zhou, K. Shung, and L. Wang, Biomed. Opt. Express **6**, 918 (2015).
15. K. Xiong, S. Yang, X. Li, and D. Xing, Opt. Lett. **43**, 1846 (2018).
16. X. Leng, W. Chapman, B. Rao, S. Nandy, R. Chen, R. Rais, I. Gonzalez, Q. Zhou, D. Chatterjee, M. Mutch, and Q. Zhu, Biomed. Opt. Express **9**, 5159 (2018).
17. H. Guo, G. Song, H. Xie, and L. Xi, Opt. Lett. **42**, 4615 (2017).
18. H. He, A. Buehler, D. Bozhko, X. Jian, Y. Cui, and V. Ntziachristos, IEEE Trans. Med. Imag. **37**, 1162 (2018).
19. B. Dong, S. Chen, Z. Zhang, C. Sun, and H. Zhang, Opt. Lett. **39**, 4372 (2014).
20. D. Cai, G. Li, D. Xia, Z. Li, Z. Guo, and S. Chen, Opt. Express **25**, 20162 (2017).
21. Y. Li, R. Lin, C. Liu, J. H. Chen, H. D. Liu, R. Q. Zheng, X. J. Gong, and L. Song, J. Biophotonics **11**, e201800034 (2018).
22. Y. Li, Z. Zhu, J. Jing, J. Chen, A. Heidari, Y. He, J. Zhu, T. Ma, M. Yu, Q. Zhou, and Z. Chen, IEEE J. Sel. Top. Quantum Electron. **25**, 7102005 (2019).
23. S. Mattison, R. Shelton, R. Maxson, and B. Applegate, Biomed. Opt. Express **4**, 1451 (2013).
24. Laser Institute of America, *American National Standard for Safe Use of Lasers ANSI Z136.1-2014* (American National Standards Institute, Inc., 2014).